A Novel Real-Time Voltage and Frequency Compensation Strategy for Photovoltaic-Based Microgrid

Hongtao Shi, *Student Member, IEEE*, Fang Zhuo, *Member, IEEE*, Hao Yi, *Member, IEEE*, Feng Wang, *Member, IEEE*, Dong Zhang, and Zhiqing Geng

***Abstract*—Weather-dependent photovoltaic (PV) system power variation may become frequent and rapid, which could be regarded as perturbation for the microgrid (MG). This perturbation would lead to voltage and frequency fluctuations and dramatically degrade the MG performances. Conventional secondary control strategy could restore the voltage and frequency after a certain time delay, but it cannot satisfy the speed demands when frequent and rapid perturbations appear. To overcome the limitation, this paper proposes a novel real-time voltage and frequency compensation strategy to suppress the fluctuations. The proposed strategy realizes voltage regulation by an adaptive virtual impedance loop and realizes frequency regulation by a virtual frequency-impedance loop. The novel real-time strategy is simple to be implemented and needless of communication; therefore, it is much more suitable for the PV-based MG. Finally, a PV-based MG is established as laboratory prototype, and experimental results validate the effectiveness of the proposed method.**

***Index Terms*—Distributed photovoltaic (PV) system, microgrid (MG), real-time control, virtual impedance.**

Nomenclature

DG	Distributed generator.
MG	Microgrid.
MPPT	Maximum power-point tracking.
PCC	Point of common coupling.
PV	Photovoltaic.
RVFCS	Real-time voltage and frequency compensation strategy.
SPWM	Sinusoidal pulsewidth modulation.
VSI	Voltage source inverter.

Manuscript received May 21, 2014; revised September 2, 2014 and October 14, 2014; accepted October 15, 2014. Date of publication November 20, 2014; date of current version May 8, 2015. This work was supported in part by the National Natural Science Foundation of China under Projects 51177130 and 51407133 and in part by the China Postdoctoral Science Foundation under Project 2014M552446.

The authors are with the State Key Laboratory of Electrical Insulation and Power Equipment, School of Electrical Engineering, Xi'an Jiaotong University, Xi'an 710049, China (e-mail: shtgyp523@163.com; zffz@mail.xjtu.edu.cn; yi_hao@mail.xjtu.edu.cn; wangfengdq110@163.com; 527876361@qq.com; gengzhiqinggzq@163.com).

Color versions of one or more of the figures in this paper are available online at http://ieeexplore.ieee.org.

Digital Object Identifier 10.1109/TIE.2014.2371434

I. Introduction

THE MG is a network which consists of DGs, loads, storage system, power quality control devices, etc. It can operate in both grid-tied mode and islanded mode [1]–[6]. VSI is usually used as the interfaced converter for DG. Droop control strategy has been widely accepted to realize power sharing among different DGs in islanded MG [7]–[9]. The performances of well-known P–ω and Q–U control strategy depend on the line impedance [10]–[12]. Consequently, virtual impedance is often applied to decouple the VSI's active and reactive powers to improve the power-sharing accuracy [13], [14].

Due to low environmental impact and government subsidies, a large percentage of distributed PV systems have been connected into MG. MPPT is a widely accepted technology to improve energy utilization efficiency [15]–[18]. Therefore, the output power of distributed PV system is intermittent and fluctuant according to real-time weather conditions, such as irradiance and temperature. Consequently, interaction between the distributed PV system and MG may occur [19]. The fluctuant PV power is regarded as one of the primary disturbances to the power flow of MG. In this condition, the voltage and frequency of the ac bus in islanded MG may deviate from their nominal values [20]–[23], leading to the deteriorative power quality of MG.

Employing a storage system in a PV system is an effective researched method to suppress the power variations of the PV system [24], [25]. However, this method still has some limitations like the following: It is costly when large capacity of storage system is needed, and the impacts from unplanned plugging-in and removing of PV system cannot be eliminated completely. Thus, in these cases, the frequency and voltage deviations would still appear.

Therefore, it is necessary to develop a control strategy for MG to improve the voltage and frequency response [26]–[32]. Some intelligent control algorithms have been applied in VSI to control the voltage and frequency [26], [27]. In [26], an adaptive neuro-fuzzy inference system is developed to stabilize the frequency and voltage of MG. In [27], the intelligent frequency control scheme based on particle swarm optimization (PSO) fuzzy tuning is designed to improve the frequency performance of MG. With these schemes, the performance of MG can be improved when facing different load changes. However, the controller design is quite complicated.

The control scheme of virtual inertia has been proposed in previous works [22], [28], known as synchronverters [28].

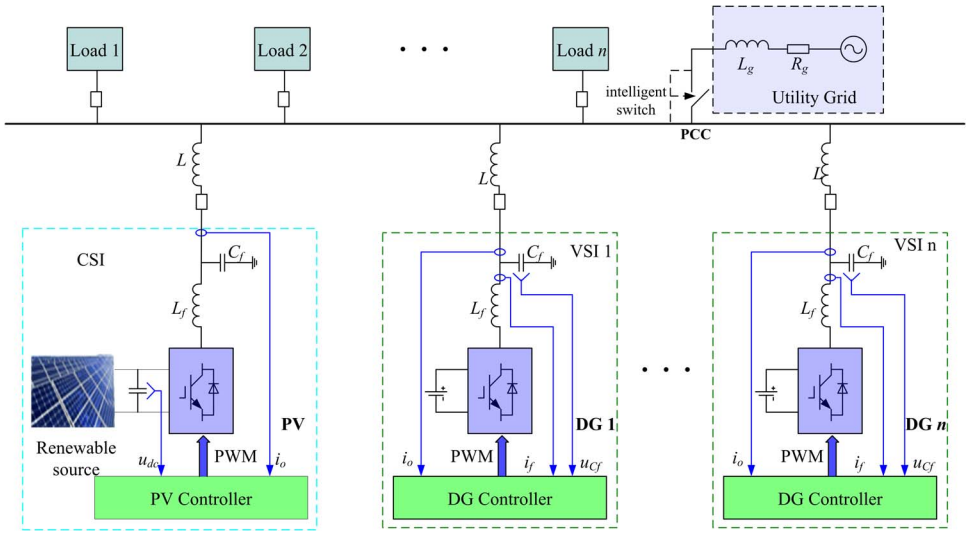

Fig. 1. Structure of MG.

However, most of the strategies are used to enhance the frequency transient response, whereas the steady-state performance cannot be improved.

Several studies have been conducted on the secondary control scheme with communication network to restore the voltage and frequency. In [29] and [30], a hierarchical control structure is proposed, and the communication network is implemented to coordinate different control levels with different bandwidth communication buses. Consequently, the voltage and frequency secondary control can be included into the control scheme. In [31], a secondary control strategy based on the cooperative control of the multiagent system is developed by using the communication network to transfer the information of one inverter and its neighbors. In [32], a secondary control is developed to restore the voltage and frequency after a certain delay time which is transferred by a communication line. To guarantee the completed power sharing, the secondary voltage and frequency restoration should be later than the droop control. Therefore, the challenge of conversional secondary control is to estimate an appropriate delay time according to the actual power fluctuation. However, it is difficult because the power fluctuation is not easy to be predicted in a practical MG. A smaller delay time means frequent communication, which may impact the power sharing performance and reduce the system reliability. To solve this issue, the delay time is usually designed large enough [29]–[32]. However, this method would lead to poor restoration performance when frequent and rapid fluctuations happen due to the power variation of the PV system.

To overcome the aforementioned issues, an RVFCS is proposed in this paper, which comprised an adaptive virtual impedance loop to regulate the voltage and an adaptive virtual frequency-impedance loop to restore the frequency (the adaptive control here comprised the outer voltage and frequency control loops, which is not referred to the nonlinear adaptive control). Compared to the conventional secondary control method, the proposed RVFCS has no need of a communication bus and designing the delay time. Therefore, the proposed RVFCS is more suitable for the PV-based MG, where the power fluctuation is frequent and rapid.

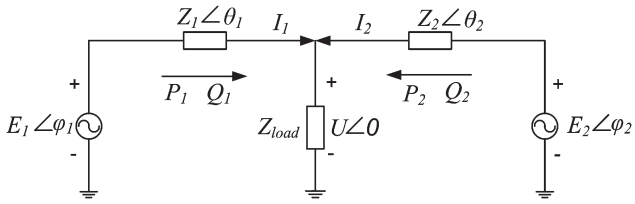

Fig. 2. Equivalent circuit for two paralleled inverters.

This paper is organized as follows. Section II briefly recalls the droop control strategy in MG, and an output VSI voltage model in the PV-based MG is derived. In Section III, the RVFCS is proposed to suppress the voltage and frequency fluctuation caused by the power variation of the PV system. In Section IV, PV-based MG is implemented. Experimental results verify the effectiveness of the proposed control scheme. Section V gives the conclusions of this paper.

II. Output Voltage Model of VSI in PV-Based MG

A. Droop Control in Islanded MG

A multi-inverter MG is shown in Fig. 1. In this system, an intelligent switch between the PCC and utility grid is used to decide the operating mode of MG by detecting the grid voltage. Most of the DGs, for instance, PV system and wind generation system, are connected into the MG through single-stage or multistage SPWM converters.

In islanded mode, each of the paralleled DGs operates as an individual voltage source, and they are power shared with a droop control scheme. Fig. 2 shows the equivalent circuit of two paralleled inverters with one common load. In the figure, $E_x(x=1,2)$ and $U_x(x=1,2)$ represent the amplitudes of the inverter output voltage and the ac bus voltage, respectively. $\varphi_x(x=1,2)$ implies the corresponding voltage phase. $Z_x(x=1,2)$ denotes the connected branch impedance, and θ is the impedance phase.

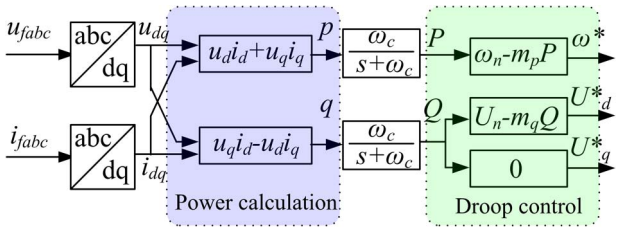

Fig. 3. Droop control scheme.

The output power of inverter 1 is expressed as [9], [33]

$$P_1 = \frac{E_1 U}{Z_1}\cos(\theta_1 - \varphi_1) - \frac{U^2}{Z_1}\cos\theta_1 \tag{1}$$

$$Q_1 = \frac{E_1 U}{Z_1}\sin(\theta_1 - \varphi_1) - \frac{U^2}{Z_1}\sin\theta_1. \tag{2}$$

As seen from the equations, the output power of the inverter is affected by the inverter output voltage and the connected branch impedance. Generally, the impedance Z can be divided into two parts

$$Z = Z_{out} + Z_{feeder}. \tag{3}$$

By using virtual impedance [13], the output impedance Z_{out} could be flexibly regulated as almost inductive or resistive. Generally, the feeder impedance Z_{feeder} is assumed small, and then, Z_{out} is dominant [13], [33]. When Z_{out} is set as mainly inductive, the output power of the inverter can be approximately expressed as [33]

$$P_1 = \frac{E_1 U}{X_1}\sin\varphi_1 \tag{4}$$

$$Q_1 = \frac{E_1 U\cos\varphi_1 - U^2}{X_1} \tag{5}$$

where X_1 is the inductance of the output impedance. In (4) and (5), if φ_1 is small $(\sin\varphi_1 \approx \varphi_1, \cos\varphi_1 \approx 1)$, the active power is proportional to φ_1, and the reactive power is proportional to the amplitude E_1 [9], [33]. For power sharing between the parallel inverters, P–ω and U–U droop control is proposed [6], [9], [11], [33], which can be expressed as

$$\omega^* = \omega_n - m_p P \tag{6}$$

$$U^* = U_n - m_q Q \tag{7}$$

where m_p and m_q are the corresponding droop gains. Then, the control scheme could be shown in Fig. 3.

The dynamic and stable performances are affected by droop gains [6], [9], [27], [33]–[35]. Under the premise of system stabilization, a larger droop gain would lead to better power sharing, at the cost of the larger voltage and frequency deviations [9], [33]. For this reason, the droop gains are always designed as a compromise of power sharing and voltage/frequency accuracy. In P–ω droop control, as shown in (6), the droop gain m_p is set as the ratio of the maximum frequency over the possible maximum active power variation

$$m_{p\max} = \frac{\Delta\omega_{\max}}{\Delta P_{\max}}. \tag{8}$$

The voltage deviation is impacted by both the voltage drop across the output impedance and the Q–U droop control [9], [34]. Therefore, the droop gain m_q is set as follows:

$$m_{q\max} = \frac{\Delta U_{\max} - I_{o\max} Z}{\Delta Q_{\max}} \tag{9}$$

where Z is the inverter output impedance. In some cases, the virtual impedance is dominant, and m_q can be set approximately as [9]

$$m_{q\max} \approx \frac{\Delta U_{\max} - I_{o\max} Z_{\text{virtual}}}{\Delta Q_{\max}}. \tag{10}$$

B. Output Voltage Model of VSI in PV-Based Islanded MG

For islanded MG in this paper, the loads are supplied by n VSIs (n is the number of VSIs) and one PV system with MPPT. To simplify the analysis, each VSI is assumed as the same capacity. In this condition, the output voltage of each VSI depends on

$$U_d^* = U_n - \frac{1}{n}\cdot m_q(Q_L - Q_{pv}) \tag{11}$$

$$U_q^* = 0 \tag{12}$$

$$\omega^* = \omega_n - \frac{1}{n}\cdot m_p(P_L - P_{pv}) \tag{13}$$

where U_d^* and U_q^* are the reference voltages of VSI, ω^* is the angular frequency reference, U_n and ω_n are their nominal values, m_p and m_q are droop gains, P_L and Q_L are the active power and reactive power of loads, and P_{pv} and Q_{pv} are the active power and reactive power of PV system.

However, the droop control would also introduce side effects for islanded MG: The voltage and frequency of the ac bus would be affected by all the VSIs with droop control. According to (11)–(13), the output voltage of VSI is determined by droop control parameters and its output power. That means that the voltage and frequency would deviate from their nominal values when the system power flow varies, and then, the power quality of the whole MG deteriorates. The power flow variation may be caused by either the load side or DG side, and it becomes inevitable when PV system is employed. Therefore, the aforementioned influences should be suppressed to maintain the voltage and frequency of the ac bus. To study the influence from the PV power fluctuation, the output voltage model of VSI is developed in this paper.

The control system of VSI is shown in Fig. 4, which contains the virtual impedance loop, voltage control loop, current control loop, decoupling link, SPWM equivalent link (K_{PWM}), and LC filter (Z_{LCdq}). L_f and C_f are the filter inductance and capacitance, R_{vir} and L_{vir} are the virtual impedances, ω_0 is the fundamental frequency, and K_{PWM} and Z_{LCdq} are the equivalent equations of the SPWM link and LC filter, respectively. $G_v(s)$ and $G_i(s)$ are transfer functions of the voltage proportional plus integral (PI) controller and current PI controller. In the figure, the feedback signals include the

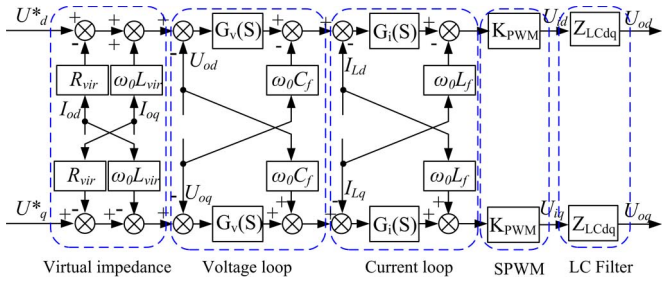

Fig. 4. Control system of VSI.

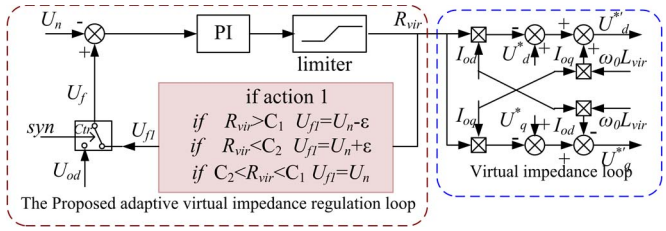

Fig. 5. Adaptive virtual impedance control scheme.

inverter output voltages (U_{od}, U_{oq}), inverter output currents (I_{od}, I_{oq}), and inductance currents (I_{Ld}, I_{Lq}). I_{od} and I_{oq} are imported into the virtual impedance loop to improve the power sharing. U_{od}, U_{oq}, I_{Ld}, and I_{Lq} are imported into the voltage control loop and current control loop, respectively, to realize the voltage control and regulation.

With the control block diagram and the droop control equations shown in (11)–(13), the output voltage model of VSI can be obtained as (detailed derivation is shown in the Appendix)

$$\begin{bmatrix} U_{od}(s) \\ U_{oq}(s) \end{bmatrix} = G(s) \cdot \begin{bmatrix} U_n - \frac{1}{n} \cdot m_q(Q_L - Q_{PV}) \\ 0 \end{bmatrix} - [Z(s)] \cdot \begin{bmatrix} I_{od}(s) \\ I_{oq}(s) \end{bmatrix} \quad (14)$$

where $G(s)$ is the voltage gain function and $[Z(s)]$ is the output impedance matrix of VSI. They can be expressed as

$$G(s) = \frac{G_{vi}(s)K_{PWM}}{L_f C_f s^2 + C_f G_i(s) K_{PWM} s + G_{vi}(s) K_{PWM} + 1} \quad (15)$$

$$[Z(s)] = G(s) \cdot \begin{bmatrix} R_{vir} + R_g & -\omega_0 L_{vir} \\ \omega_0 L_{vir} & R_{vir} + R_g \end{bmatrix} \quad (16)$$

where $R_g = (G_i(s)K_{PWM} + sL_f/G_v(s)G_i(s)K_{PWM})$ and $G_{vi}(s) = G_v(s)G_i(s)$.

As described in (13), the frequency of VSI is related to P_{pv}, m_p, and n, while there are numerous factors affecting the VSI voltage, as shown in (14) and (16), such as the following: Q_{pv}, m_q, $G(s)$, $[Z(s)]$, I_{od}, I_{oq}, and n.

According to the VSI model defined in (13), (14), and (16), this problem could be solved if the parameters of VSI could be regulated adaptively.

As seen from the voltage model in (13), (14), and (16), the degree of frequency deviation depends on the change of active power and the droop gain m_p which is usually set as a small value in VSI. Therefore, the frequency deviation could be eliminated by the minor adjustment of m_p, while the output impedance voltage drop would change as the variation of active current and then lead to the voltage amplitude deviation. Compared to the voltage deviation caused by reactive power variation, the voltage deviation resulting from the active current fluctuation plays a greater part. In this case, although the voltage can be restored by regulating the m_q, this adjustment process would result in the major change of m_q, which may lead to poor reactive power sharing, because the Q–U droop control is more difficult to be realized in MG [9], [10].

Consequently, in this paper, an adaptive virtual impedance scheme is used to restore the voltage, and meantime, m_q is maintained to be an appropriate value to ensure the reactive power sharing performance [6], [9], [10].

III. Proposed RVFCS for MG

A. Adaptive Virtual Impedance Strategy

In this adaptive control scheme, an additional virtual impedance loop is implemented to adaptively generate the value of virtual impedance, as shown in Fig. 5.

The adaptive virtual impedance scheme here would operate in two modes according to the working state: "Preparation mode" for offline VSI to get ready for plugging into the MG and "Regulating mode" for online VSI to compensate voltage deviations caused by PV power variations.

Preparation mode: In this case, the output of the PI controller (virtual impedance) should be limited within a suitable range to avoid the negative influence when the inverter is plugging into the MG. This function is realized by the "if action 1" module.

In this condition, the signal "syn" equals to "0." The output voltage of VSI equals to its nominal value, and the output of the PI controller (virtual impedance) is sustaining a random value at first. If the virtual impedance R_{vir} is greater than the upper threshold C_1, the feedback voltage U_f will equal to a voltage that is smaller than the nominal value $U_n - \varepsilon$ (where ε is a small positive constant value and it can be set as $0.1\ U_n \sim 0.5\ U_n$). The output of the adaptive control loop will be decreased and vice versa, where C_2 is the lower threshold. Then, the virtual impedance R_{vir} will be regulated within a suitable scope $[C_2, C_1]$. The value limitation can be set as the impedance estimation of the other MG-tied inverters.

Regulating mode: In this case, VSI has been connected into the islanded MG. With droop control, its output voltage may deviate from the nominal value if power flow varies, like when the output power of the PV system fluctuates.

The signal "*syn*" is set as "1," and the feedback voltage U_f equals to the VSI output voltage U_{od}. The virtual impedance would be regulated in real time by the deviation of voltage, which can be expressed as

$$R_{vir} = k_{rp}(U_{od} - U_n) + \frac{1}{T_{ri}} \int (U_{od} - U_n) dt \quad (17)$$

where k_{rp} and T_{ri} are the proportion gain and integration time of the PI controller.

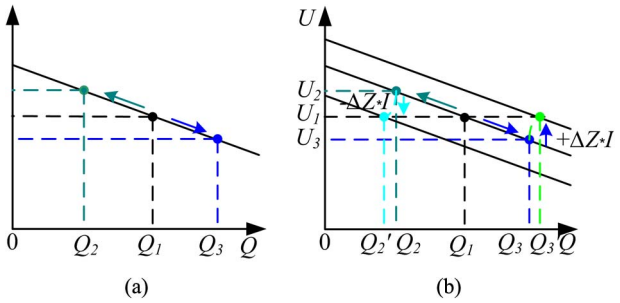

Fig. 6. Q–V characteristic of droop control. (a) With traditional droop control. (b) With adaptive virtual impedance control loop.

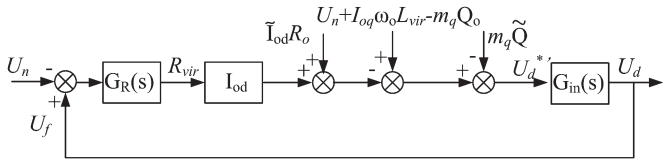

Fig. 7. Voltage control diagram.

In this case, the VSI voltage references could be modified as

$$U_d^{*'} = U_d^* - \left(k_{rp}(U_{od} - U_n) + \frac{1}{T_{ri}}\int (U_{od} - U_n)dt\right) \cdot i_{od} + \omega_0 L_{vir} \cdot i_{oq} \tag{18}$$

$$U_q^{*'} = 0 - \left(k_{rp}(U_{od} - U_n) + \frac{1}{T_{ri}}\int (U_{od} - U_n)dt\right) \cdot i_{oq} - \omega_0 L_{vir} \cdot i_{od} \tag{19}$$

where $U_d^{*'}$ and $U_q^{*'}$ are the modified voltage references.

With the adaptive virtual impedance scheme, the output impedance of VSI can be regulated according to the voltage.

The effect of the proposed virtual impedance compensation scheme is illustrated in Fig. 6. With the traditional droop control, the voltage will deviate from its nominal value when power changes, as shown in Fig. 6(a) (from (Q_1, U_1) to (Q_2, U_2) or (Q_3, U_3)), whereas with the adaptive virtual impedance, the voltage deviation would be eliminated, as shown in Fig. 6(b) (from (Q_2, U_2) to (Q_2', U_1) or from (Q_3, U_3) to (Q_3', U_1)).

As discussed earlier, the VSI output voltage is controlled by the nested droop control and adaptive virtual impedance control loop. In order to guarantee the stability of the system and the power sharing performance, the inner droop control loop should be faster than the outer adaptive virtual impedance loop. In other words, at the beginning of regulation, the droop control should play the major role to share the power. After that, the adaptive virtual impedance plays the major role to restore the voltage.

Fig. 7 shows the voltage control diagram, which consists of the adaptive virtual impedance controller $G_R(s)$, droop control, and inner voltage control loop $G_{in}(s)$ (the detailed control diagram of the inner loop is shown in Fig. 4). In Fig. 7, the output current is divided into two parts: the constant part I_{od} and the variable part $\widetilde{I_{od}}$. Similarly, the reactive power is divided into two parts: the constant part Q_o and the variable part $\widetilde{Q}$. $\widetilde{I_{od}}R_o$ and $\widetilde{Q}$ are regarded as the disturbances that impact the voltage.

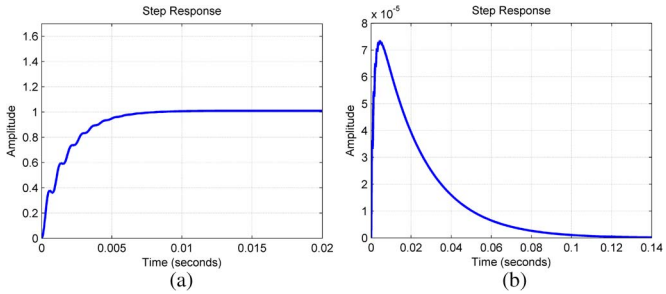

Fig. 8. Unit step response of (a) inner loop and (b) outer voltage adjustment control loop.

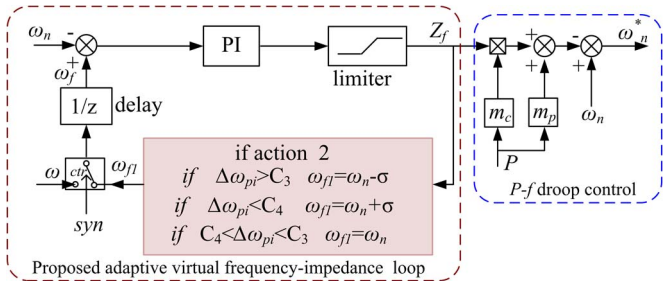

Fig. 9. Adaptive virtual frequency-impedance control scheme.

By using the outer voltage adjustment control loop (the adaptive virtual impedance loop), the voltage deviation caused by $\widetilde{I_{od}}$ and $\widetilde{Q}$ can be eliminated. The transfer function $\widetilde{Q} - U_{od}$ can be expressed as follows:

$$U_{od} = \frac{G(s)m_q}{1 + G_R(s)G(s)I_{od}}\tilde{Q} \tag{20}$$

where $G(s)$ is the voltage transfer gain, the expression of which is shown in (15). $G_R(s)$ is the function of the adaptive virtual impedance controller.

Fig. 8 shows the unit step response of the inner and outer control loops. In the design of the inner loop, the crossover frequency f_c of the current loop is generally set as 0.1 f_s (f_s is the switching frequency) to 0.2 f_s. The crossover frequency of the voltage loop is much smaller than the f_c. Consequently, the step response time can be set as a few milliseconds, as shown in Fig. 8(a). The outer loop is used to eliminate the response of disturbance. To guarantee that the system is stable and to keep a certain stability margin, the step response time of the outer loop can be set as at least ten times larger than that of the inner loop, which is shown in Fig. 8(b). This criterion can be used to determine the value of k_{rp} and T_{ri}.

B. Adaptive Virtual Frequency-Impedance Compensation Strategy

In order to suppress the frequency variation caused by the PV power variation, the notion of virtual frequency-impedance is introduced here. The corresponding frequency compensation scheme could be depicted as Fig. 9, which is composed by a PI controller and one "if action" module. Similar with the adaptive voltage compensation scheme in the last section, the frequency compensation scheme here would also operate in two modes according to the working state: "Preparation mode" for offline

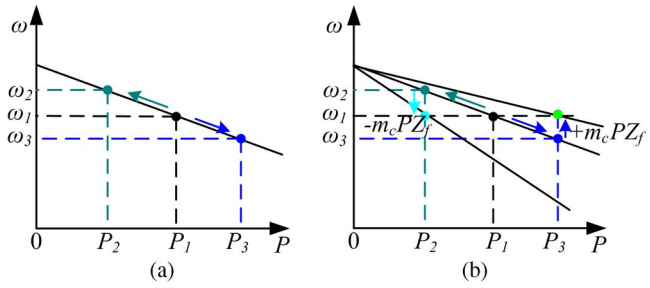

Fig. 10. P–ω characteristic of droop control. (a) With traditional droop control. (b) With adaptive frequency compensation control loop.

VSI to get ready for plugging into the MG and "Regulating mode" for online VSI to compensate the frequency deviation caused by PV power variation.

Preparation mode: In this case, the signal "syn" is set as "0." Similar to the adaptive voltage compensation scheme, the PI output Z_f should be limited to ensure the frequency of the output voltage to keep the range reasonable around the nominal value. Then, the VSI could be smoothly plugged into MG when needed. This function should be fulfilled by the "if action 2" module in Fig. 9, and its working principle could be described as follows: When Z_f is greater than the upper threshold C_3, the feedback frequency ω_f is set as $\omega_n - \sigma$ (σ is a small positive constant value which ranges from $0.1\omega_n$ to $0.5\omega_n$) to decrease Z_f; when Z_f is less than the lower threshold C_4, the feedback frequency ω_f is set as $\omega_n + \sigma$ to increase Z_f. The upper and lower limits (C_3 and C_4) should be determined by the following relation:

$$|m_{p\max} - m_c \cdot Z_f|\,\Delta P_{\max} \le \Delta\omega_{\max}. \tag{21}$$

Regulating mode: In this case, the signal "syn" is set as "1." VSI has been plugged into the MG. The frequency of VSI ω would be fed back as ω_f, and the virtual frequency-impedance would be regulated in real time to eliminate frequency deviation caused by PV power variations. The corresponding compensation scheme could be expressed as

$$\omega^* = \omega_n - m_p P - m_c P \cdot Z_f \tag{22}$$

where m_c is a compensation coefficient which is smaller than the droop coefficient m_p. Z_f is the frequency-impedance defined in this paper which can be expressed by

$$Z_f = k_{cp}(\omega - \omega_n) + \frac{1}{T_{ci}}\int(\omega - \omega_n)dt \tag{23}$$

where k_{cp} and T_{ci} are the proportion gain and integration time of the PI controller.

The effect of the proposed virtual frequency compensation scheme is illustrated in Fig. 10. Obviously, without the frequency compensation scheme, frequency deviation happens when power changes for traditional P–ω droop control, as shown in Fig. 10(a) (from (P_1,ω_1) to (P_2,ω_2) or (P_3,ω_3)), whereas with the proposed adaptive frequency compensation scheme, this frequency deviation could be avoided as shown in Fig. 10(b) (from (P_2,ω_2) to (P_2,ω_1) or from (P_3,ω_3) to (P_3,ω_1)).

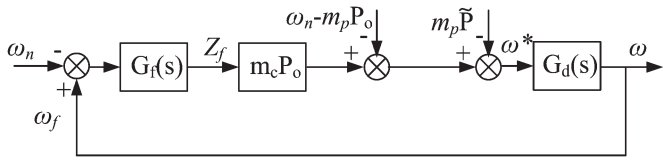

Fig. 11. Frequency control diagram.

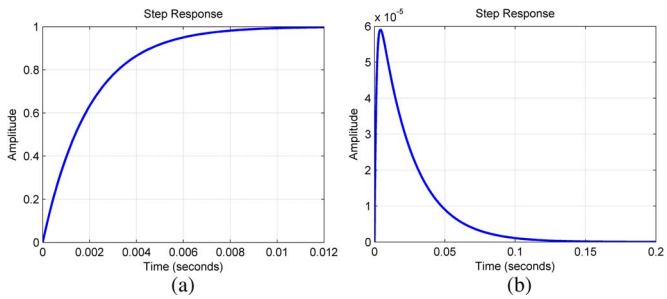

Fig. 12. Unit step response of (a) inner loop and (b) outer adaptive frequency-impedance compensation loop.

As discussed earlier, the frequency is controlled by the nested droop control and adaptive frequency-impedance control loop. In order to guarantee the stability of the system and power sharing performance, the inner droop control loop should be faster than the outer adaptive virtual impedance loop.

Fig. 11 shows the frequency control diagram, which consists of the adaptive frequency-impedance controller $G_f(s)$, f–ω droop control, and delay link $G_d(s)$. In Fig. 11, the active power is divided into two parts: the constant part P_o and the variable part $\widetilde{P}$, where $\widetilde{P}$ is regarded as the disturbance to impact the frequency. The delay link $G_d(s)$ is defined as the transfer function $\omega*$-to-ω, which represents the following links: dq transform, SPWM, and LC filter; it could be expressed as follows:

$$\omega = G_d(s)\omega^* = \frac{1}{T_d s + 1}\omega^*. \tag{24}$$

The transfer function $\widetilde{P}$-to-ω can be expressed as follows:

$$\omega = \frac{G_d(s)m_p}{1 + G_f(s)G_d(s)m_c P_o}\tilde{P} \tag{25}$$

where $G_f(s)$ is the function of the adaptive frequency-impedance controller, which can be expressed as

$$G_f(s) = k_{fp} + \frac{1}{T_{fi}\cdot s} \tag{26}$$

where k_{fp} and T_{fi} are the proportion gain and integral time of the PI controller.

Fig. 12 shows the unit step response of the inner and outer control loops. The response time of the inner loop is usually a few milliseconds, as shown in Fig. 12(a). The outer loop is used to eliminate the response of disturbance. To guarantee that the system is stable and to keep a certain stability margin, the unit step response time of the outer adaptive frequency-impedance compensation loop can be set as at least ten times larger than that of the inner loop, as shown in Fig. 12(b). This criterion can be used to determine the value of k_{fp} and T_{fi}.

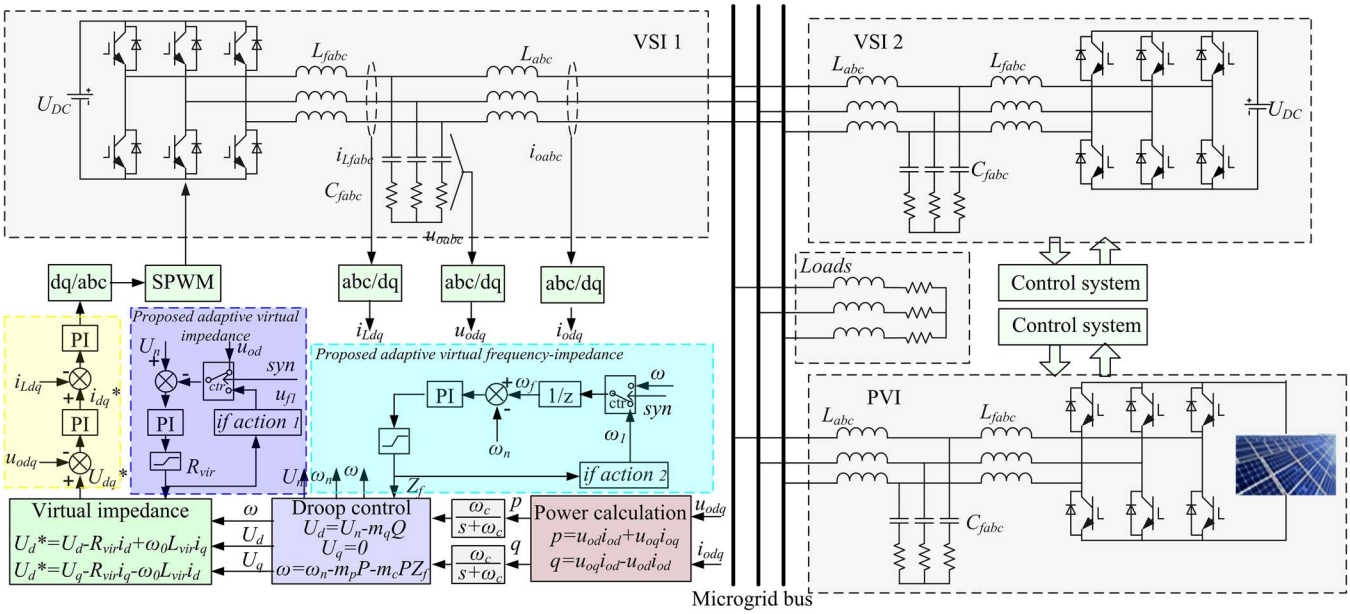

Fig. 13. Control scheme of PV-based islanding MG.

The parameter design criterion aforementioned is generic. The actual values of these parameters should be designed according to both the power rating of the system and the actual operating mode of MG.

When the proposed RVFCS method is applied in different rated MGs, the droop gains and virtual impedance of VSI should be designed as the power rating of VSI and the feeder impedance, etc. Based on the stability analysis, the voltage and current control loops are designed. Then, according to the inner loop speed of response, the outer adjustment voltage and frequency control loops (adaptive virtual impedance loop and adaptive frequency-impedance loop) can be developed.

With the adaptive voltage and frequency compensation strategy introduced earlier, the deviation of bus voltage, in both amplitude and frequency, could be suppressed in real time, without any communication networks. The whole control system could be depicted as Fig. 13.

IV. Experimental Verification

The effectiveness of the proposed RVFCS is verified through a testing islanded MG in the laboratory, as shown in Fig. 14. The islanded MG contains two VSIs, one PV generator, and their common load. The two VSIs, with an individual dc source at the dc side, work under voltage source mode to maintain the bus voltage of MG, while the PV generator works under current source mode to achieve better MPPT and, meanwhile, to simulate power perturbation through output power variation. The detailed parameters are listed in Table I. Three types of tests are carried out to check the performances of the proposed adaptive strategy on suppressing the influences from power variations.

1) Plugging-In and Plugging-Off of PV System: The PV system is interfaced by a current source-type converter. At the moment that it starts or stops injecting active current to the load,

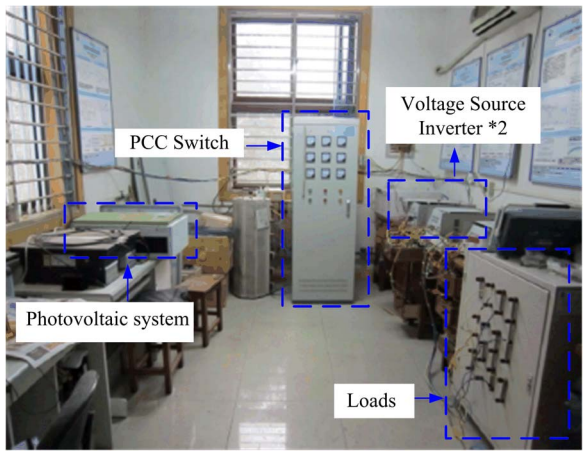

Fig. 14. Photograph of MG.

TABLE I
Parameters of the MG Used in Experiment

Parameter	Value	Unit
Microgrid voltage	120	V
Microgrid frequency	50	Hz
Switching frequency of VSI	10	kHz
Filter inductance of VSI	0.72	mH
Filter capacitor of VSI	60	μF
The power rating of PV system	2.5	kW
The power rating of each VSI	3	kW
Droop gain m_p of VSI	1e-3	rad/s/w
Droop gain m_q of VSI	1.2e-3	V/var
k_{vp}, T_{vi}	0.08, 0.52	-
k_{ip}, T_{ii}	0.015, 100	-
k_{rp}, T_{ri}	0.002, 3	-
k_{fp}, T_{fi}	0.05, 30	-

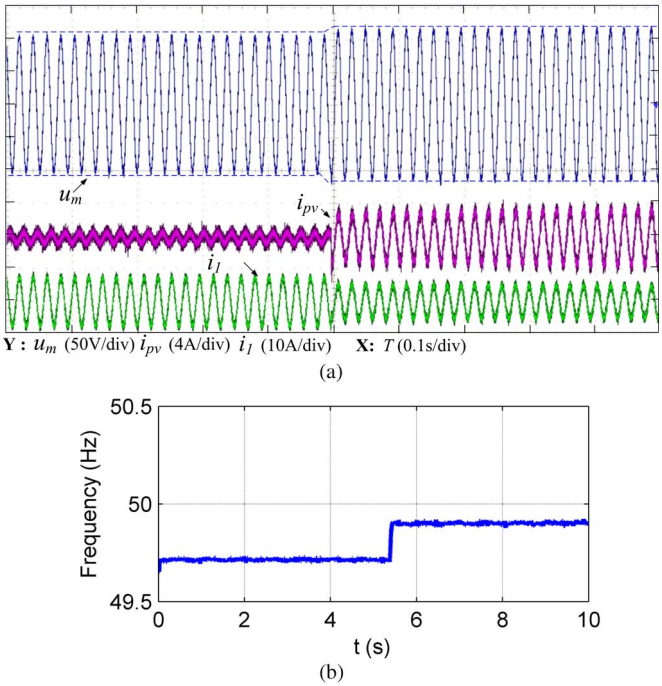

Fig. 15. Experimental results in case (1) without RVFCS. (a) Voltage and current waveforms of ac bus. (b) Frequency curve of ac bus.

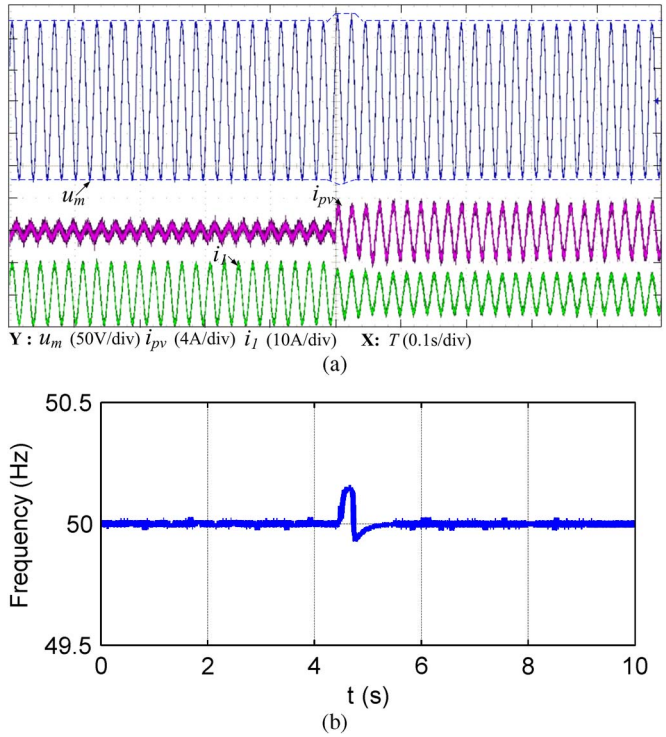

Fig. 16. Experimental results in case (1) with RVFCS. (a) Voltage and current waveforms of ac bus. (b) Frequency curve of ac bus.

power flow varies in the islanded MG, and the performances of the other two VSIs would be affected.

As shown in Fig. 15, when no compensation scheme is implemented, the amplitude [in (a)] and frequency [in (b)] of MG bus voltage would deviate from their nominal values when the PV system is plugged in. The frequency curve in Fig. 15(b) is plotted through online measurement and offline calculation in Matlab (the voltage of the ac bus is sampled and saved by the digital phosphor oscilloscope Tektronix DPO4034 with sampling frequency f_{sample}. Then, the voltage data are imported into Matlab, where a specialized program is used to calculate the frequency. This program can count the sampling number n for every fundamental period. Then, the frequency f equals to $f_{sample}/(n-1)$.

In contrast, when the proposed RVFCS is implemented, the deviations could be eliminated in real time as shown in Fig. 16(a) and (b). It can be seen from the figures that voltage and frequency deviations reach almost 6 V and 0.2 Hz after the power variation, respectively, but they come back to their nominal values through a short-time regulating process.

When the PV system is removed from the MG, the voltage and frequency deviations reach almost 10 V and 0.3 Hz. After the regulation of RVFCS, the voltage and frequency can be restored to their nominal values, as shown in Fig. 17.

2) Power Fluctuation Resulting From Load Variation: Aside from PV power fluctuations, the load change is another factor affecting the power flow in MG. The VSIs should adjust their output power to balance the sources and loads once load change happens. This means that the voltage and frequency are readjusted in the islanded MG with droop control. Fig. 18 shows the voltage and frequency waveforms when the load step increases. It can be seen from the figures that the voltage and the frequency deviate from their nominal values at the moment of

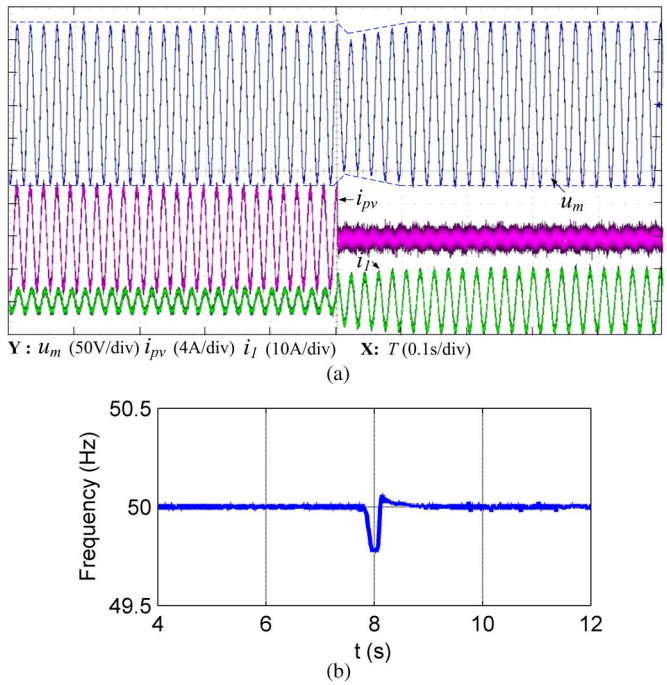

Fig. 17. Experimental results when PV system is removed from MG with RVFCS. (a) Voltage and current waveforms of ac bus. (b) Frequency curve of ac bus.

load change. The deviations reach about 5 V in amplitude and 0.16 Hz in frequency. With RVFCS, the voltage and frequency could restore to their nominal values in real time, as shown in Fig. 18(a) and (b).

3) Fluctuation of PV Power: Due to the weather variation, the output power of the PV system has the characteristic of fluctuation. In this case, with respect to EN50530 [36], [37],

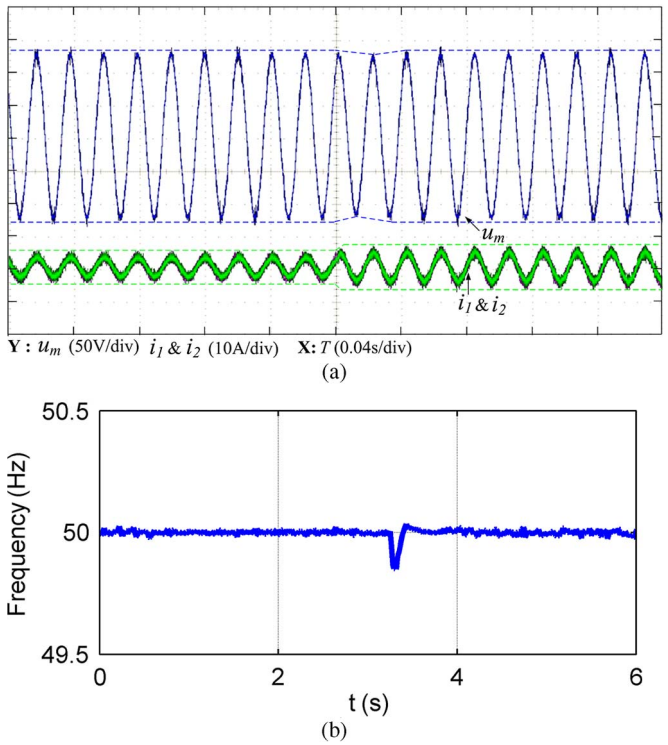

Fig. 18. Experimental results in case (2) with RVFCS. (a) Voltage and current waveforms of ac bus. (b) Frequency curve of ac bus.

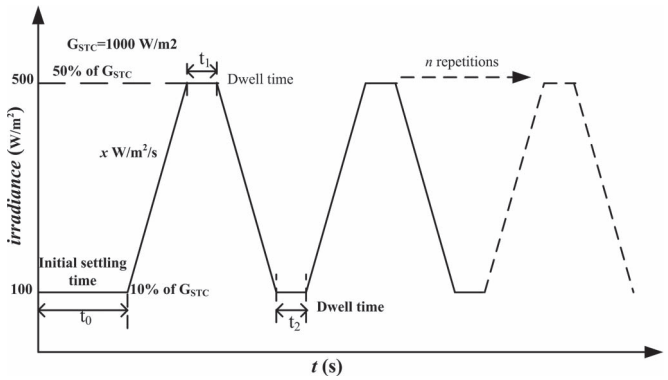

Fig. 19. Ramp sequence with n repetitions (10%–50% of G_{rated}).

a fluctuant output current of the PV system is injected into the islanded MG.

The standard EN50530 includes a series of irradiance ramp such as 0, 5, and 100 W/m^2/s (the rated irradiance G_{rated} is set as 1000 W/m^2) [37]. Namely, the ramp is 0, 0.005, and 0.1 G_{rated}/s. The test in EN50530 can be conducted with two levels: Low to medium $(100 \sim 500$ W/m$^2)$ and medium to high $(300 \sim 1000$ W/m$^2)$ [37], [38]. In each test, a ramp sequence with n repetitions is used, as shown in Fig. 19 [37], [38].

In order to test the proposed method under the rapid PV power fluctuation, in our experiment, the irradiance is set as 0.1 G_{rated}/s. The test level is set as low to medium (10% to 50% of G_{rated}). MPPT time is set as 1 s.

Fig. 20(a) shows the PV current in the test. In the figure, the rated current of PV system I_{rate} is 10 A. The test level is 10% to 50% of I_{rated} (corresponding to 10% to 50% of G_{rated}). The

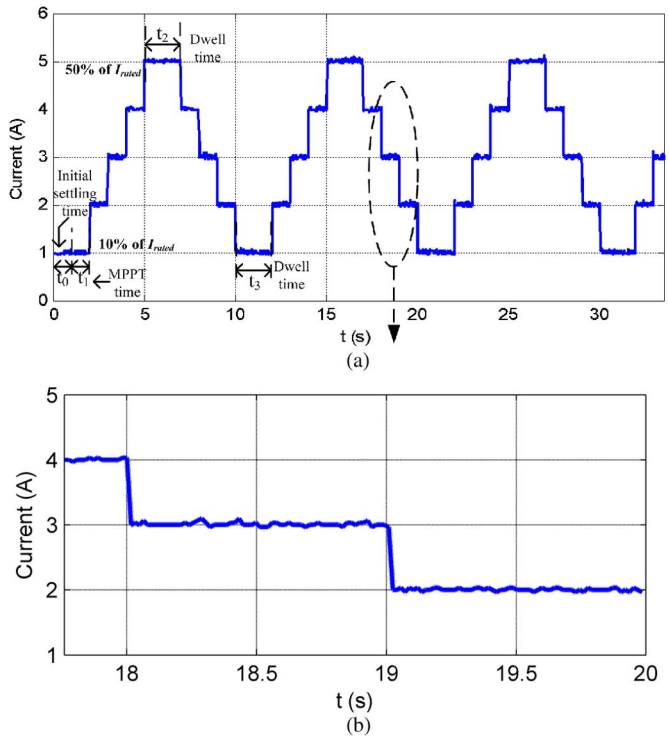

Fig. 20. PV current in test. (a) PV current (low to medium). (b) Current variation in 17.7–20 s.

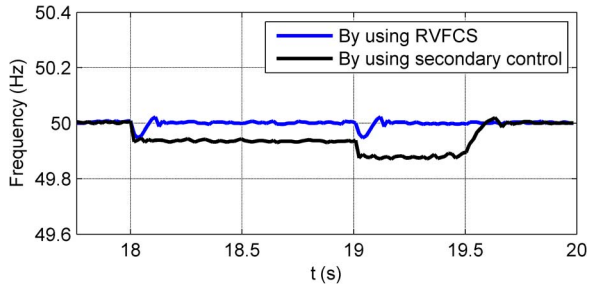

Fig. 21. Frequency curves in case (3) with traditional control strategy and RVFCS.

initial time is set as 1 s. After the initial time, the PV current variation is 1 A/s due to the MPPT time.

As discussed in this paper, the fluctuation of PV current would lead to MG bus voltage and frequency variations. In order to outline the superiority of the proposed RVFCS, a traditional secondary control strategy [29]–[32] was also tested to make comparisons. The delay time of the traditional secondary control strategy is set as 1.5 s and given by the communication bus in the tests. Fig. 20(b) shows the current curve in 17.7–20 s, and Figs. 21 and 22 show the corresponding voltage and frequency curves.

It can be seen from the figures that, for the case of using the conventional secondary control scheme with delay time, the voltage and frequency fluctuations cannot be suppressed in time. The frequency and voltage bias are about 0.05 Hz and 1.5 V in 18 s and about 0.1 Hz and 3 V in 19 s. The voltage and frequency are restored after the certain delay time. However, in practical applications, the delay time is difficult to set because the power fluctuations in a real environment are frequent and

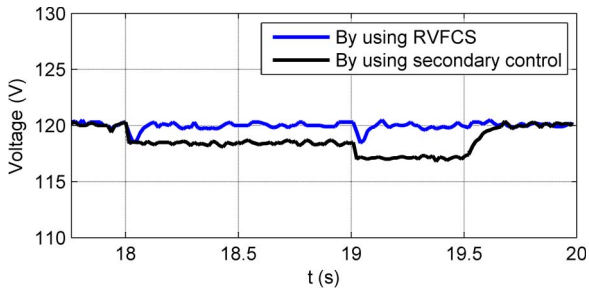

Fig. 22. Voltage curves in case (3) with traditional control strategy and RVFCS.

random, which are not easy to be predicted. A smaller delay time means frequent communication, which may impact the power sharing performance and reduce the system reliability. Consequently, the delay time is generally set to be large enough to guarantee that the system is stable. It can be seen from the figures that a large delay time leads to an obvious voltage and frequency restoration delay.

In contrast, with the proposed RVFCS, no communication system is needed, and no delay time needed to be designed. The voltage and frequency can be restored in real time.

V. Conclusion

The voltage and frequency may deviate from their nominal values due to power fluctuation in MG. The conversional secondary control strategy restores the voltage and frequency after certain delay time with the communication bus, but the delay time is difficult to be set because the power variation is not easy to be predicted. An unsuitable delay would decrease the performance of the system. In this paper, a novel RVFCS for PV-based MG is proposed based on the output voltage model of VSI. With the proposed method, neither delay time nor communication bus needs to be considered, and the voltage and frequency deviations could be eliminated in real time by using an adaptive virtual impedance loop and a virtual frequency-impedance loop, respectively. This proposed method is more applicable to the PV-based MG, in which the power fluctuation is more frequent and rapid. The experiment results show the effectiveness of the proposed method.

Appendix

For the control system of VSI shown in Fig. 4, the voltage before the LC filter can be expressed as

$$\begin{aligned}\begin{bmatrix} U_{id}(s) \\ U_{iq}(s) \end{bmatrix} &= A \cdot \begin{bmatrix} U_d^*(s) \\ U_q^*(s) \end{bmatrix} - A \cdot \begin{bmatrix} R_{vir} & -\omega_0 L_{vir} \\ \omega_0 L_{vir} & R_{vir} \end{bmatrix} \\ &\cdot \begin{bmatrix} I_{od}(s) \\ I_{oq}(s) \end{bmatrix} - \begin{bmatrix} A & B \\ -B & A \end{bmatrix} \cdot \begin{bmatrix} U_{od}(s) \\ U_{oq}(s) \end{bmatrix} \\ &- \begin{bmatrix} G_i(s)\frac{U_{dc}}{2} & \omega_0 L_f \\ -\omega_0 L_f & G_i(s)\frac{U_{dc}}{2} \end{bmatrix} \cdot \begin{bmatrix} I_{Ld}(s) \\ I_{Lq}(s) \end{bmatrix} \end{aligned} \tag{27}$$

where $A = G_v(s)G_i(s)(U_{dc}/2)$,$B = \omega_0 C_f G_i(s)(U_{dc}/2)$, and $G_v(s)$ and $G_i(s)$ are transfer functions of the voltage controller and current controller, respectively.

The voltages across the filter inductance can be expressed as

$$\begin{bmatrix} U_{id}(s) \\ U_{iq}(s) \end{bmatrix} = \begin{bmatrix} U_{od}(s) \\ U_{oq}(s) \end{bmatrix} + \begin{bmatrix} sL_f & -\omega_0 L_f \\ \omega_0 L_f & sL_f \end{bmatrix} \begin{bmatrix} I_{Ld}(s) \\ I_{Lq}(s) \end{bmatrix}. \tag{28}$$

In dq coordinate, the inductance currents I_{Ld} and I_{Lq} and the output currents I_{od} and I_{oq} satisfy that

$$\begin{bmatrix} I_{Ld}(s) \\ I_{Lq}(s) \end{bmatrix} = \begin{bmatrix} I_{od}(s) \\ I_{oq}(s) \end{bmatrix} + \begin{bmatrix} sC_f & -\omega_0 C_f \\ \omega_0 C_f & sC_f \end{bmatrix} \begin{bmatrix} U_{od}(s) \\ U_{oq}(s) \end{bmatrix}. \tag{29}$$

Combining (27)–(29), the transfer function between the reference voltage and the output voltage can be expressed as

$$\begin{bmatrix} U_{od}(s) \\ U_{oq}(s) \end{bmatrix} = G(s) \begin{bmatrix} U_d^*(s) \\ U_q^*(s) \end{bmatrix} - [Z(s)] \begin{bmatrix} I_{od}(s) \\ I_{oq}(s) \end{bmatrix} \tag{30}$$

where $G(s)$ is the voltage gain function and $[Z(s)]$ is the output impedance matrix of VSI.

References

[1] Y. Li, D. M. Vilathgamuwa, and P. C. Loh, "Design, analysis and real time testing of a controller for multibus microgrid system," *IEEE Trans. Power Electron.*, vol. 19, no. 5, pp. 1195–1204, Sep. 2004.

[2] J. M. Carrasco *et al.*, "Power electronic systems for the grid integration of renewable energy sources: A survey," *IEEE Trans. Power Electron.*, vol. 53, no. 4, pp. 1002–1016, Aug. 2006.

[3] M. Liserre, R. Theodorescu, and F. Blaabjerg, "Stability of photovoltaic and wind turbine grid-connected inverters for a large set of grid impedance values," *IEEE Trans. Power Electron.*, vol. 21, no. 1, pp. 263–272, Jan. 2006.

[4] S. Anand and B. G. Fernandes, "Reduced order model and stability analysis of low voltage dc microgrid," *IEEE Trans. Ind. Electron.*, vol. 60, no. 11, pp. 5040–5049, Nov. 2013.

[5] R. Majumder, "Some aspects of stability in microgrids," *IEEE Trans. Power Syst.*, vol. 28, no. 3, pp. 3243–3252, Aug. 2013.

[6] C. N. Rowe, T. J. Summers, R. E. Betz, D. J. Cornforth, and T. G. Moore, "Arctan power-frequency droop for improved microgrid stability," *IEEE Trans. Power Electron.*, vol. 28, no. 8, pp. 3747–3759, Aug. 2013.

[7] Q.-C. Zhong, "Robust droop controller for accurate proportional load sharing among inverters operated in parallel," *IEEE Trans. Ind. Electron.*, vol. 60, no. 4, pp. 1281–1290, Apr. 2013.

[8] K. T. Tan, P. L. So, Y. C. Chu, and M. Z. Q. Chen, "Coordinated control and energy management of distributed generation inverters in a microgrid," *IEEE Trans. Power Del.*, vol. 28, no. 2, pp. 704–713, Apr. 2013.

[9] W. Yao, M. Chen, J. Matas, J. M. Guerrero, and Z. Qian, "Design and analysis of the droop control method for parallel inverters considering the impact of the complex impedance on the power sharing," *IEEE Trans. Ind. Electron.*, vol. 58, no. 2, pp. 576–588, Feb. 2011.

[10] J. Kim, J. M. Guerrero, P. Rodriguez, R. Teodorescu, and K. Nam, "Mode adaptive droop control with virtual output impedances for an inverter-based flexible ac microgrid," *IEEE Trans. Power Electron.*, vol. 26, no. 3, pp. 689–701, Mar. 2011.

[11] J. He, Y. Li, J. M. Guerrero, F. Blaabjerg, and J. C. Vasquez, "An islanding microgrid power sharing approach using enhanced virtual impedance control scheme," *IEEE Trans. Power Electron.*, vol. 28, no. 11, pp. 5272–5282, Nov. 2013.

[12] C.-T. Lee, C.-C. Chu, and P.-T. Cheng, "A new droop control method for the autonomous operation of distributed energy resource interface converters," *IEEE Trans. Power Electron.*, vol. 28, no. 4, pp. 1980–1993, Apr. 2013.

[13] J. He and Y. W. Li, "Analysis, design, implementation of virtual impedance for power electronics interfaced distributed generation," *IEEE Trans. Ind. Electron.*, vol. 47, no. 6, pp. 2525–2538, Nov. 2011.

[14] J. He, Y. Li, and F. Blaabjerg, "Flexible microgrid power quality enhancement using adaptive hybrid voltage and current controller," *IEEE Trans. Ind. Electron.*, vol. 61, no. 6, pp. 2784–2794, Jun. 2014.

[15] B. N. Alajmi, K. H. Ahmed, S. J. Finney, and B. W. Williams, "Fuzzy-logic-control approach of a modified hill-climbing method for maximum power point in microgrid standalone photovoltaic system," *IEEE Trans. Power Electron.*, vol. 26, no. 4, pp. 1022–1030, Apr. 2011.
[16] A. K. Abdelsalam, A. M. Massoud, S. Ahmed, and P. Enjeti, "High-performance adaptive perturb and observe MPPT technique for photovoltaic-based microgrids," *IEEE Trans. Power Electron.*, vol. 26, no. 4, pp. 1010–1021, Apr. 2011.
[17] S.-M. Chen, T.-J. Liang, and K.-R. Hu, "Design, analysis, implementation of solar power optimizer for dc distribution system," *IEEE Trans. Power Electron.*, vol. 28, no. 4, pp. 1764–1772, Apr. 2013.
[18] H. Valderrama-Blavi, J. M. Bosque, F. Guinjoan, L. Marroyo, and L. Martinez-Salamero, "Power adaptor device for domestic dc microgrids based on commercial MPPT inverters," *IEEE Trans. Ind. Electron.*, vol. 60, no. 3, pp. 1191–1203, Mar. 2013.
[19] A. Yazdani and P. P. Dash, "A control methodology and characterization of dynamics for a photovoltaic (PV) system interfaced with a distribution network," *IEEE Trans. Power Del.*, vol. 24, no. 3, pp. 1538–1551, Jul. 2009.
[20] J. M. Guerrero, M. Chandorkar, T.-L. Lee, and P. C. Loh, "Advanced control architectures for intelligent microgrids-part I: Decentralized and hierarchical control," *IEEE Trans. Ind. Electron.*, vol. 60, no. 4, pp. 1254–1262, Apr. 2013.
[21] J. M. Guerrero, P. C. Loh, T.-L. Lee, and M. Chandorkar, "Advanced control architectures for intelligent microgrids-Part II: Power quality, energy storage, ac/dc microgrids," *IEEE Trans. Ind. Electron.*, vol. 60, no. 4, pp. 1263–1270, Apr. 2013.
[22] N. Soni, S. Doolla, and M. C. Chandorkar, "Improvement of transient response in microgrids using virtual inertia," *IEEE Trans. Power Del.*, vol. 28, no. 3, pp. 1830–1838, Jul. 2013.
[23] S. M. Ashabani and Y. A.-R. I. Mohamed, "General interface for power management of micro-grids using nonlinear cooperative droop control," *IEEE Trans. Power Syst.*, vol. 28, no. 3, pp. 2929–2941, Aug. 2013.
[24] A. Elmitwally and M. Rashed, "Flexible operation strategy for an isolated PV-diesel microgrid without energy storage," *IEEE Trans. Energy Convers.*, vol. 26, no. 1, pp. 235–244, Mar. 2011.
[25] J. M. Bosque, H. Valderrama-Blavi, M. Munoz, X. Mzixe, and P. Garces, "Increased dynamics adaptor to incorporate energy sources in PV-based dc microgrids," in *Proc. EPE-PEMC Conf.*, 2010, pp. 18–24.
[26] H. Bevrani and S. Shokoohi, "An intelligent droop control for simultaneous voltage and frequency regulation in islanded microgrids," *IEEE Trans. Smart Grid*, vol. 4, no. 3, pp. 1505–1513, Sep. 2013.
[27] H. Bevrani, F. Habibi, P. Babahajyani, M. Watanabe, and Y. Mitani, "Intelligent frequency control in an ac microgrid: Online PSO-based fuzzy tuning approach," *IEEE Trans. Smart Grid*, vol. 3, no. 4, pp. 1935–1944, Dec. 2012.
[28] Q.-C. Zhong, P.-L. Nguyen, Z. Ma, and W. Sheng, "Self-synchronized synchronverters: Inverters without a dedicated synchronization unit," *IEEE Trans. Power Electron.*, vol. 29, no. 2, pp. 617–630, Feb. 2014.
[29] J. M. Guerrero, J. C. Vasquez, J. Matas, L. G. de Vicuña, and M. Castilla, "Hierarchical control of droop-controlled ac and dc microgrids-A general approach toward standardization," *IEEE Trans. Ind. Electron.*, vol. 58, no. 1, pp. 158–172, Jan. 2011.
[30] A. Bidram and A. Davoudi, "Hierarchical structure of microgrids control system," *IEEE Trans. Smart Grid*, vol. 3, no. 4, pp. 1963–1976, Dec. 2012.
[31] A. Bidram, A. Davoudi, F. L. Lewis, and Z. Qu, "Secondary control of microgrids based on distributed cooperative control of multi-agent systems," *IET Gener. Transmiss. Distrib.*, vol. 7, no. 8, pp. 822–831, Aug. 2013.
[32] J. C. Vsquez, J. M. Guerrero Zapata, M. Savaghebi, J. Eloy-Garcia, and R. Teodorescu, "Modeling, analysis, design of stationary reference frame droop controlled parallel three-phase voltage source inverters," *IEEE Trans. Ind. Electron.*, vol. 60, no. 4, pp. 1271–1280, Apr. 2013.
[33] J. M. Guerrero, L. G. de Vicuña, J. Matas, M. Castilla, and J. Miret, "Output impedance design for parallel-connected UPS inverters with wireless load-sharing control," *IEEE Trans. Ind. Electro.*, vol. 52, no. 4, pp. 1126–1135, Aug. 2005.
[34] L. Mihalache, "Paralleling control technique with no intercommunication signals for resonant controller-based inverters," in *Conf. Rec. IEEE IAS Annu. Meeting*, 2003, pp. 1882–1889.
[35] P. H. Divshali, S. H. Hosseinian, and M. Abedi, "A novel multi-stage fuel cost minimization in a VSC-based microgrid considering stability, frequency voltage constraints," *IEEE Trans. Power Syst.*, vol. 28, no. 2, pp. 931–939, Apr. 2013.
[36] B. Bletterie, R. Bruendlinger, and S. Spielauer, "Quantifying dynamic MPPT performance under realistic conditions first test results-The way forward," in *Proc. 21st EU PV Conf.*, 2006, pp. 2347–2351.
[37] R. Brndlinger, N. Henze, H. Häberlin, A. Bergmann, and F. Baumgartner, "prEN 50530-The new European standard for performance characterisation of PV inverters," in *Proc. 24th EU PV Conf.*, 2009, pp. 3105–3109.
[38] H. Haeberlin and P. Schaerf, "New procedure for measuring dynamic MPP-tracking efficiency at grid-connected PV inverters," in *Proc. 24th EU PV Conf.*, 2009, pp. 1–7.

Hongtao Shi (S'13) was born in Hebei, China, in 1984. He received the B.S. and M.S. degrees in electrical engineering from Ningxia University, Ningxia, China, in 2008 and 2011, respectively. He is currently working toward the Ph.D. degree in the Power Electronics and Renewable Energy Research Center, Department of Electrical Engineering, Xi'an Jiaotong University, Xi'an, China.

His research interests include modeling and control for distributed generation systems.

Fang Zhuo (M'00) was born in Shanghai, China, in 1962. He received the B.S. degree in automatic control and the M.S. and Ph.D. degrees in automation and electrical engineering from Xi'an Jiaotong University, Xi'an, China, in 1984, 1989, and 2001, respectively.

He was an Associate Professor at Xi'an Jiaotong University in 1996 and a Full Professor in power electronics and drives in 2004. Then, he worked as a supervisor of Ph.D. students. His research interests include power electronics, power quality, active power filter, reactive power compensation, inverters for distributed power generation, etc. He is the key finisher of four projects sponsored by the National Natural Science Foundation of China and more than 40 projects in cooperation with companies from industry. He has four pending patent applications.

Dr. Zhuo is a member of the China Electrotechnical Society, Automation Society, and Power Supply Society. He is also the Power Quality Professional Chairman of the Power Supply Society in China. He was the recipient of four provincial-and ministerial-level science and technology advancement awards.

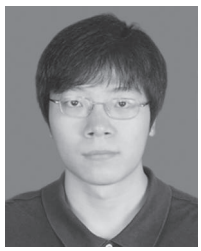

Hao Yi (S'10–M'13) was born in Shaanxi, China, in 1984. He received the M.S. degree and the Ph.D. degree in electrical engineering from Xi'an Jiaotong University, Xi'an, China, in 2010 and 2013, respectively.

He is currently a member of the School of Electrical Engineering, Xi'an Jiaotong University. His research interests include modeling and control of power quality problems and distributed generators in the microgrid.

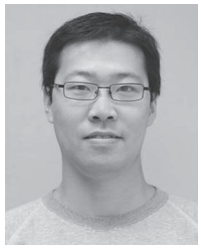

Feng Wang (S'08–M'13) received the B.S., M.S., and Ph.D. degrees in electrical engineering from Xi'an Jiaotong University, Xi'an, China, in 2005, 2009, and 2013, respectively.

In November 2013, he joined Xi'an Jiaotong University as a Postdoctoral Fellow. His research interests include dc/dc conversion and digital control of switched converters, particularly in renewable energy generation fields.

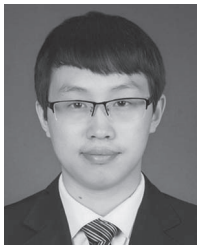

Dong Zhang was born in Hebei, China, in 1990. He received the B.S. degree in electrical engineering from Xi'an Jiaotong University, Xi'an, China, in 2012, where he is currently working toward the M.S. degree in the Department of Electrical Engineering.

His research interests include power quality problems and inverters for distributed power generation.

Zhiqing Geng was born in Shaanxi, China, in 1989. He received the B.S. degree in electrical engineering from Southwest Jiaotong University, Chengdu, China, in 2012. He is currently working toward the M.S. degree in the Department of Electrical Engineering, Xi'an Jiaotong University, Xi'an, China.

His research interests include active power filters and control techniques for paralleled inverters.